Branching ratio between resonant and non-resonant ionization of xenon evaluated from photoelectron angular distributions

2012 Phys. Scr. 86 035303

(http://iopscience.iop.org/1402-4896/86/3/035303)

IOP Publishing Physica Scripta
Phys. Scr. **86** (2012) 035303 (5pp) doi:10.1088/0031-8949/86/03/035303

Branching ratio between resonant and non-resonant ionization of xenon evaluated from photoelectron angular distributions

M Goto[1] **and K Hansen**

Department of Physics, University of Gothenburg, 41296 Gothenburg, Sweden

E-mail: motoshi-goto@riken.jp and klavs.hansen@physics.gu.se

Received 9 March 2012
Accepted for publication 8 August 2012
Published 30 August 2012
Online at stacks.iop.org/PhysScr/86/035303

Abstract
Photoelectron imaging of xenon gases ionized with a femtosecond 388 nm pulse reveals three ionization processes: resonant and non-resonant multi-photon ionization and autoionization. The relative yield of the first two was evaluated from the deconvolution of their angular distribution for the specific electron energy, which includes the electron production via the $3h\nu$–$5p^5(^2P^\circ_{1/2})6s$ resonance. The non-resonant process gains in importance with increasing laser intensity and accounts for 50% of the ionization yield at 30 TW cm^{-2}.

PACS numbers: 32.80.Fb, 32.80.Rm, 32.80.Zb, 32.90.+a

(Some figures may appear in colour only in the online journal)

1. Introduction

Electron imaging techniques have proven to be powerful tools for analyzing angle-dependent photoelectron distributions [1]. They have been successfully applied for studies on atom–light interaction using short intense laser pulses and rare gases [2–6] to observe angular distributions of above threshold ionization (ATI) [7] and Freeman resonances, caused by the ponderomotive energy (U_p) shift of Rydberg states [8]. Kaminski *et al*, for example, have reported excitation of xenon for the wavelength range of 500–650 nm and shown that ionization via an intermediate *d* state gives a significant contribution of *f* character angular distributions to the spectrum [9]. It is widely known that non-resonant ionization also plays an important role and that this ionization mechanism gives a broad electron spectrum with a specific angular distribution [10].

In this paper, we report on the ionization of xenon excited with a short intense 388 nm (3.2 eV) laser pulse with intensities below 38 TW cm^{-2} for which, to our knowledge, no report has been published previously. The aim is to examine to what extent an analysis of the entire photoelectron angular distributions will allow one to establish a branching ratio of two ionization paths. We examine the competition between the ionization via the $3h\nu$–$5p^5(^2P^\circ_{1/2})6s$ (hereafter $3h\nu$–$6s'$) resonance and the non-resonant ionization, taking advantage of the difference in angular distributions between them in the analysis. The evolution of the angular distribution with the laser intensity can be explained in terms of the change in branching of the two paths. Although we will not go into the theoretical interpretation of this result, it clearly shows that this analysis works and gives important hints for the understanding of the ionization mechanism.

2. Experiment

Our experimental setup has been described elsewhere [11]. In brief, a 388 nm pulse was obtained by the frequency doubling of the fundamental pulse of our laser (775 nm, 150 fs). The remaining 775 nm photons were removed with dichroic mirrors. This frequency-doubled pulse was focused into a chamber where xenon gas was introduced with a needle valve. The generated electrons were accelerated and then detected under an electric focusing condition [12] with a chevron

[1] Present address: Atomic, Molecular and Optical Physics Laboratory, RIKEN, 2-1 Hirosawa, Wako, Saitama 351-0198, Japan.

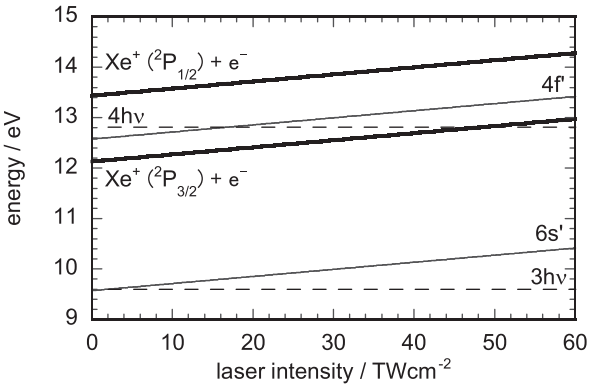

Figure 1. Energy level of xenon interacting with a laser field for the wavelength of 388 nm (3.2 eV), illustrating the level shift of the two ionic states of $^2P_{1/2}$ and $^2P_{3/2}$ and two Rydberg states for the $^2P_{1/2}$ core, together with those of 3 and $4h\nu$.

configuration micro-channel plate detector in combination with a phosphor screen. The phosphor screen luminescence was monitored with a charge-coupled device camera without synchronizing with the laser shots.

Typical pressures inside the chamber were 1×10^{-6} mbar with a background pressure of 4×10^{-7} mbar. Due to the relatively high background pressure, it was necessary to reduce the contribution of electrons generated from the background gas. For this purpose, an image recorded without xenon in the chamber was also measured under the same experimental conditions. This spectrum was subtracted from the corresponding image measured with xenon. However, the fluctuations in shot-by-shot pulse energy often caused incomplete subtraction of the background signal, even under nominally identical conditions. This will be considered in the analysis.

The images obtained this way were inverted following the procedure reported in [13] and then calibrated by means of the ATI peak separation that was identified with the photon energy, to give the photoelectron spectrum. The laser intensity was calibrated relative to the pulse energy where the $4h\nu$–$5p^5(^2P^\circ_{1/2})4f$ (hereafter $4h\nu$–$4f'$) resonance appeared (see below). The duration was estimated to be 200 fs. The laser polarization direction was set with a polarizer to be parallel to the detector plane. Throughout this paper, $\theta = 0$ indicates the polarization direction.

3. Results and discussion

In this section, we discuss the identification of the ionization processes and then give the analysis of the angular distributions.

3.1. Identification of the ionization processes

The energy levels of xenon interacting with a 388 nm (3.2 eV) laser field are shown in figure 1. Information about the energy levels was obtained from the NIST atomic spectra database. Xenon has an ionization energy (IE) at 12.13 eV corresponding to the ion core $^2P_{3/2}$ and a second threshold at 13.44 eV corresponding to the ion core $^2P_{1/2}$. Both energies are values for zero U_p. Thus, the energy of a four-photon process exceeds only the lower of these two thresholds.

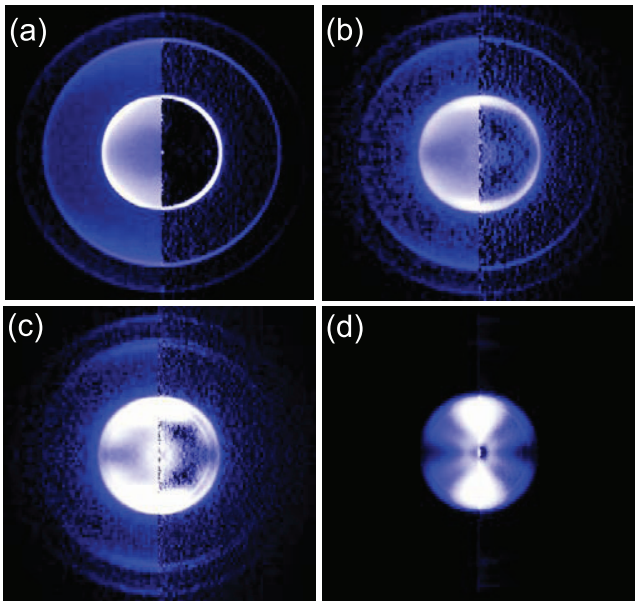

Figure 2. Raw photoelectron images (left half of each frame) and the corresponding inverted images up to the kinetic energy of 4 eV (right half) for four different laser intensities: (a) 2.1, (b) 12, (c) 22 and (d) 38 TW cm^{-2}. The colour scale is logarithmic and covers three orders of magnitude in amplitude except (c), whose colour scale is saturated for display purposes. The laser polarization is in the vertical direction.

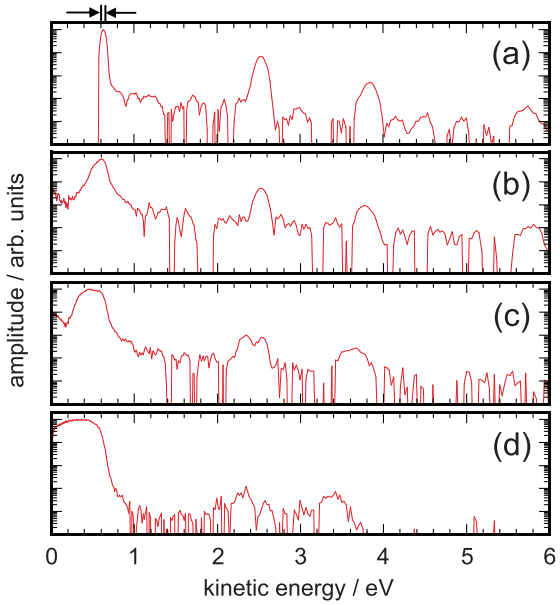

Figure 3. Semi-log plot of the angle-integrated photoelectron spectra of the inverted images shown in figure 2. The amplitude is normalized to the highest ordinate. The energy region indicated on top of the figure will be used in the angle-resolved analysis later.

For intensities below 38 TW cm^{-2}, which is the highest used in this study, two resonances are active: $3h\nu$–$6s'$ and $4h\nu$–$4f'$ for the intensities of 2.1 and 16 TW cm^{-2}, respectively. In the field-free condition, the former state is located at 9.57 eV and the latter at 12.58 eV.

Photoelectron images for four different intensities and their corresponding angle-integrated spectra are shown in figures 2 and 3, respectively. It is evident from these figures that the spectra are highly dependent on the intensity.

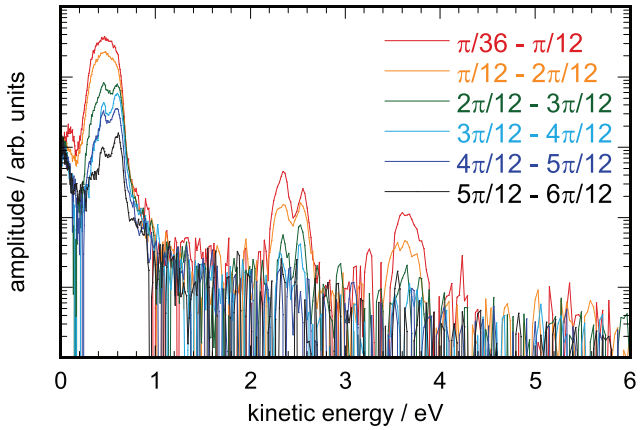

Figure 4. Angle-dependence analysis of the spectrum shown in figure 3(c) for every $\pi/12$. The region from $\theta = 0$ to $\pi/36$ is excluded due to the noise generated in the inversion [13].

For the lowest intensity, which matches the intensity for the $3h\nu$–6s′ resonance, the spectrum is composed of three peaks centered at 0.64, 2.52 and 3.84 eV. Knowing the values of IE and U_p (30 meV), they can be assigned to ionization via the resonance into the $^2P_{3/2}$ ion core in a (3 + 1) photon process, into the $^2P_{1/2}$ ion core and ATI into the $^2P_{3/2}$ ion core in a (3 + 2) photon process, respectively.

The difference between the spectra recorded at the two lowest intensities is minor except for the peak broadening due to the U_p shift for the higher of the two intensities. However, a comparison of the lowest energy peak reveals the surprising fact that the angular distribution is changed; in particular, the amplitude for $\theta = 0$ is obviously increased (see also figures 5(a) and (d) for an easier comparison). This observation will be the subject of the next subsection.

In the image of the second highest intensity (figure 2(c)), we recognize that another resonant structure, represented by a smaller ring, appears in addition to the $3h\nu$–6s′ resonance. This structure is not seen in the angle-integrated spectra but, as expected from the image, the angle-resolved spectra displayed in figure 4 clearly show a peak at the energy of 0.46 eV for θ larger than $\pi/6$. The reason for this angular dependence is that for small θ, non-resonant ionization is the dominant process, as will be explained below. If this peak originates in a resonance at $3h\nu$, its energy must be 9.29 eV, measured from the ground state and in the absence of any electric field. But no state exists at this energy and hence the autoionzation from a $4h\nu$ resonance state is a more reasonable suggestion. Furthermore, the 4f′ state is a good candidate for this channel since this state lies 0.44 eV above the $^2P_{3/2}$ threshold. This explanation is supported by the results of [14], where autoionization of these states after four-photon excitation was detected.

In addition to the autoionization process, the 2.34 eV peak observed in the spectra gets a contribution from ionization via this 4f′ state with the final state $^2P_{1/2}$. Therefore, the 4f′ state plays a role in an intermediate state both for the autoionization and for the (4 + 1) photon ionization.

Another feature that is clearly seen in the images for the two highest intensities is a broad and strong signal in the polarization direction. This is reasonably identified as a non-resonant process because of its width.

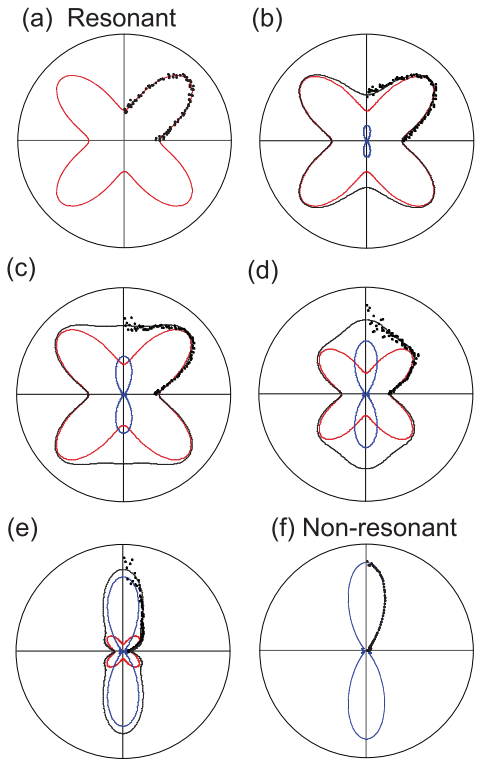

Figure 5. Polar plot of the angular distributions. The polarization is in the vertical direction. Frames (a)–(e) show the angular distributions for five different intensities: 2.1, 2.9, 5.3, 12 and 22 TW cm^{-2}, respectively. The energy interval used is from 0.60 to 0.66 eV, as indicated in figure 3. The data in frames (a), (d), (e) correspond to the ones shown in figures 2(a)–(c), respectively. Frame (f): the energy interval 0.10–0.40 eV for the image shown in figure 2(d). Dots indicate experimental data for every 1° and the amplitude of the strongest point is normalized to unity. In (a) and (f), lines indicate fitting curves with equation (1). Black lines used in (b)–(e): fitting of the plot with equation (2). Red and blue lines indicate the first and the second terms in this equation, respectively. The first two of these are derived from the distributions shown in (a) and (f), respectively. The contribution of c_3 in equation (2), which was calculated from $\int c_3\, d\theta / \int D_{obs}(\theta)\, d\theta$ and found to be less than 10% for the intensities below 10 TW cm^{-2} and 25% on average for those above, is already subtracted.

For the highest intensity, which is 2.5 times higher than the intensity giving rise to the $4h\nu$–4f′ resonance, the non-resonant process dominates the image and the resonances become much less pronounced. This tendency is also observable in figure 3, which illustrates that the highest intensity spectrum yields the strongest relative signal below electron energies of 0.64 eV (corresponding to the $3h\nu$–6s′ resonance) with no significant signal from the resonances. Thus, the non-resonant ionization becomes the dominant path as the intensity increases.

3.2. Evaluation of the branching ratio between the resonant and the non-resonant ionization

As shown above, the angular distribution of the smallest energy ring structure shown in figure 2(a) changes with laser intensity. To discuss this observation quantitatively, the dependence on the laser intensity of the distribution in the region 0.60–0.66 eV, denoted by $D_{obs}(\theta)$, is shown in figures 5(a)–(e). The energy interval corresponds roughly

Table 1. Fitting coefficients for $D_r(\theta)$ and $D_n(\theta)$ for equation (1).

Parameters	$D_r(\theta)$	$D_n(\theta)$
a	0.695(13)	0.125(1)
β_2	0.261(4)	2.890(20)
β_4	−0.832(4)	2.576(20)
β_6	0.003(6)	1.575(18)
β_8	0.063(6)	−0.159(17)

to the resolution at this energy, as defined by the size of the luminescence signal on the phosphor screen. The corresponding laser intensity range for 388 nm is below 5.0 TW cm^{-2}, which will be important for the later discussion of the branching ratio of resonant and non-resonant processes.

The experimental results indicate that at the lowest intensity, which gives rise to the $3h\nu$–6s′ resonance, $D_{obs}(\theta)$ has its maximum at $\theta = \pi/4$. At present no results are available in the literature for (3 + 1)-photon ionization via the 6s′ state and only the (3 + 1)-photon ionization via the $5p^5(^2P^\circ_{1/2})7s$ (7s′) state has been reported [15]. That report has shown that 7s′ resonant intermediate ionization path provides a similar angular distribution as that displayed in figure 5(a). We thus conclude that $D_{obs}(\theta)$ gets no contribution from the non-resonant ionization.

When the intensity is increased, $D_{obs}(\theta)$ changes systematically. The amplitude at $\theta = 0$ increases and the relative amplitude at $\theta = \pi/4$ decreases. At the highest intensity (figure 5(e)), $D_{obs}(\theta)$ has its maximum at $\theta = 0$ and the amplitude at $\theta = \pi/4$ is rather small. Compared to the other $D_{obs}(\theta)$, it bears a strong resemblance to the distribution in figure 5(f), which is the angular distribution of the image shown in figure 2(d) which, we remind the reader, is the distribution from below the 4f′ autoionization energy threshold. In other words, figure 5(f) represents the distribution where the non-resonant process is the dominant channel. From these observations we conclude that the ionization mechanism changes from resonant to non-resonant as the laser intensity increases, at least for the energy region treated here.

For a quantitative understanding of this switching mechanism, we decompose $D_{obs}(\theta)$ into the contributions from the two paths. The analysis requires numerical expressions of the angular distributions of the resonant and the non-resonant ionization, denoted by $D_r(\theta)$ and $D_n(\theta)$, respectively. We employ the distribution of figure 5(a) for the former and that of figure 5(f) for the latter, and fit them by a superposition of Legendre polynomials [16],

$$D(\theta) = a[1 + \Sigma\beta_{2n} P_{2n}(\cos\theta)]. \quad (1)$$

The fitting curves are also given in figures 5(a) and (f), showing that with $n \leqslant 4$ these curves reproduce the experimental data well. The fitting coefficients for these are summarized in table 1.

The deconvolution is carried out with the equation

$$D_{obs}(\theta) = c_1 D_r(\theta) + c_2 D_n(\theta) + c_3. \quad (2)$$

The incomplete subtraction of background signal, mentioned above, requires the use of a non-zero and angle-independent fit parameter c_3.

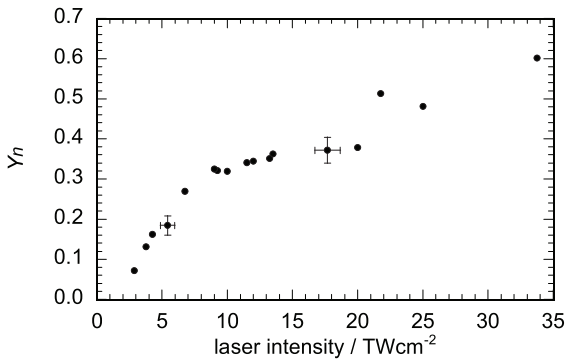

Figure 6. Y_n obtained from the scheme discussed in the text. The vertical error bars at 5.5 and 17.5 TW cm^{-2} indicate the reproducibility in the region indicated by the horizontal error bars.

For completeness we note that the resonant and non-resonant angular distributions are very similar, although not identical, to the distributions one obtains from the angular distribution of a $|p_z|^2$ orbital (for the non-resonant signal) and the angular distribution of a probability distribution $|d_{yz}|^2 + a|s|^2$ for the resonant process, with a being a small number. It is not clear to us if this is a coincidence.

The results of this deconvolution are also shown in figures 5(b)–(e), indicating that the fitting is satisfactory. This confirms that the evolution of $D_{obs}(\theta)$ with laser power is explained in terms of the change in the branching ratio.

The branchings into the resonant and the non-resonant paths, Y_r and Y_n, are calculated as

$$Y_r = \frac{c_1 \int D_r(\theta)\, d\theta}{c_1 \int D_r(\theta)\, d\theta + c_2 \int D_n(\theta)\, d\theta}, \quad (3)$$

$$Y_n = 1 - Y_r. \quad (4)$$

Y_n versus the intensity is plotted in figure 6.

The figure confirms that Y_n increases with *the peak laser intensity*. Let us discuss this result for two intensity regions: below and above 5.0 TW cm^{-2}, corresponding to the electron energy of 0.66 eV, which is the highest energy of the analysed region. The resonant ionization takes place at the intensity of 2.1 TW cm^{-2}, which is the lowest intensity in this study and produces the electrons at 0.64 eV. Above this peak intensity, the ionization is non-resonant and Y_n must consequently increase with increasing peak energy. The behaviour of the branching ratio in this intensity region therefore conforms to our expectations. At higher intensities, on the other hand, one may expect that the branching would be independent of the peak intensity, because the detected electrons originate during periods of intensities below 5.0 TW cm^{-2}, given the energy window which we measure. An increase in intensity may cause a larger degree of ionization but all electrons originating at fluences beyond 5.0 TW cm^{-2} will arrive outside the energy window. However, our results provide evidence that a higher peak intensity indeed causes an enhancement of the non-resonant process. The reason for this is not clear. One may speculate that the ionization process depends on the rate of increase of the electric field, and that the process cannot be considered instantaneous from the point of view of the duration of the laser pulse.

4. Conclusion

We have presented photoelectron spectra of xenon excited and ionized with a 200 fs, 388 nm pulse at different fluences. The differences in angular distributions of the resonant and the non-resonant channels allowed us to decompose the angular distributions at different laser intensities and to determine the intensity dependence of the branching ratios between the two channels. It was found that the relative yield of non-resonantly ionized atoms increases with increasing peak laser intensity. The study suggests that a detailed analysis of angular distributions may be a tool for determining multiphoton ionization mechanisms in other species.

Acknowledgments

This work has been supported by the Swedish Research Council (VR) through Stiftelsen för Internationalisering av högre utbildning och forskning (STINT).

References

[1] Helm H, Bjerre N, Dyer M J, Huestis D L and Saeed M 1993 *Phys. Rev. Lett.* **70** 3221
[2] Schyja V, Lang T and Helm H 1998 *Phys. Rev.* A **57** 3692
[3] Wiehle R, Witzel B, Helm H and Cormier E 2003 *Phys. Rev.* A **67** 063405
[4] Rudenko A, Zrost K, Schröter C D, de Jesus V L D, Feuerstein B, Moshammer R and Ullrich J 2004 *J. Phys. B: At. Mol. Opt. Phys.* **37** L407
[5] Maharjan C M, Alnaser A S, Litvinyuk I, Ranitovic P and Cocke C L 2006 *J. Phys.* B **39** 1955
[6] Marchenko T, Muller H G, Schafer K J and Vrakking M J J 2010 *J. Phys.* B **43** 185001
[7] Agostini P, Fabre F, Mainfray G and Petite G 1979 *Phys. Rev. Lett.* **42** 1127
[8] Freeman R R, Bucksbaum P H, Milchberg H, Darack S, Schumacher D and Geusic M E 1987 *Phys. Rev. Lett.* **59** 1092
[9] Kaminski P, Wiehle R, Renard V, Kazmierczak A, Lavorel B, Faucher O and Witzel B 2004 *Phys. Rev.* A **70** 053413
[10] Heim H and Dyer M J 1994 *Phys. Rev.* A **49** 2726
[11] Kjellberg M, Johansson O, Jonsson F, Bulgakov A V, Bordas C, Campbell E E B and Hansen K 2010 *Phys. Rev.* A **81** 023202
[12] Eppink A T J B and Parker D H 1997 *Rev. Sci. Instrum.* **68** 3477
[13] Bordas C, Paulig F, Helm H and Huestis D L 1996 *Rev. Sci. Instrum.* **67** 2257
[14] Blazewicz P R, Stockdale J A D, Miller J C, Efthimiopoulos T and Fotakis C 1987 *Phys. Rev.* A **35** 1092
[15] Bordas C, Dyer M J, Fairfield T, Helm H and Kulander K C 1995 *Phys. Rev.* A **51** 3726
[16] Reid K L 2003 *Annu. Rev. Phys. Chem.* **54** 397